sustainability

MDPI

Article

Bond Performance of Corroded Steel Reinforcement and Recycled Coarse Aggregate Concrete after Freeze–Thaw Cycles

Xutong Huang [1], Tian Su [2,3,4,5], Jinxu Wang [1], Fubo Cao [1,*] and Chenxia Wang [1,*]

[1] School of Civil Engineering, Inner Mongolia University of Science & Technology, Baotou 014017, China
[2] School of Civil and Architectural Engineering, Shandong University of Technology, Zibo 255000, China
[3] School of Civil Engineering, Wuhan University, 8 Donghu South Road, Wuhan 430072, China
[4] China Railway 11 Bureau Group Co., Ltd., 277 Zhongshan Road, Wuhan 430061, China
[5] International College, Krirk University, No. 3 Soi Ramintra 1, Ramintra Road, Anusaowaree, Bangkhen, Bangkok 10220, Thailand
* Correspondence: caofubo@imust.edu.cn (F.C.); wangchenxia@imust.edu.cn (C.W.); Tel./Fax: +86-0472-5951577 (F.C.)

Abstract: Freeze–thaw cycles and steel reinforcement corrosion can damage the properties of concrete structures in a frigid marine environment. In this paper, experimental and analytical research on the freeze–thaw resistance of recycled coarse aggregate concrete (RAC) and the bond performance of corroded steel reinforcement and RAC after freeze–thaw cycles was conducted. The results showed that the ultimate bond strength decreases with increasing freeze–thaw cycles and steel reinforcement corrosion rates, and the bond strength decreases more rapidly under the coupled effect of freeze–thaw cycles and steel reinforcement corrosion. Additionally, the quantitative analysis of the relationships between the ultimate bond strength and different freeze–thaw cycles and steel reinforcement corrosion rates was conducted through the relativity analysis, and analysis results revealed that freeze–thaw cycles have a more pronounced effect on the ultimate bond strength than steel reinforcement corrosion. A modified bond–slip prediction model of corroded steel reinforcement and RAC after freeze–thaw cycles was established, and the model exhibited better agreement with the test data of this and other research, demonstrating its rationality and applicability. These research results can provide experimental and analytical support for freeze–thaw-resistant design and bond performance prediction of RAC structures in a frigid marine environment.

Keywords: recycled coarse aggregate concrete; steel reinforcement corrosion; freeze–thaw cycles; bond performance; modified bond–slip prediction model

check for updates

Citation: Huang, X.; Su, T.; Wang, J.; Cao, F.; Wang, C. Bond Performance of Corroded Steel Reinforcement and Recycled Coarse Aggregate Concrete after Freeze–Thaw Cycles. *Sustainability* **2023**, *15*, 6122. https://doi.org/10.3390/su15076122

Received: 10 February 2023
Revised: 24 March 2023
Accepted: 30 March 2023
Published: 2 April 2023

Copyright: © 2023 by the authors. Licensee MDPI, Basel, Switzerland. This article is an open access article distributed under the terms and conditions of the Creative Commons Attribution (CC BY) license (https://creativecommons.org/licenses/by/4.0/).

1. Introduction

In recent decades, the worldwide construction industry rapidly developed, leading to environmental degradation and the gradual scarcity of sand and stone resources. Many types of wastes, such as demolished construction waste [1,2], glass [3,4], marble [5,6], PET [7], coal bottom ash [8], and waste tires [9], can be converted to recycled aggregate through crushing treatments. Recycled aggregate can replace natural aggregate and can be used in the casting of new concrete, and this concrete is called recycled aggregate concrete (RAC). This application contributes to sustainable development and environmental conservation.

The carrying capacity of RAC structures is greatly affected by the mechanical properties of steel reinforcement and RAC [10,11], and the bond performance of steel reinforcement and RAC also have a significant effect on the carrying capacity of RAC structures [12,13]. Additionally, the bond performance is the foundation of practical design, the basis of numerical simulation, and is of great value to engineering and academic research [12]. Hence, the bond performance of steel reinforcement and RAC has become a global research hotspot, and the results of previous research showed that the bond performance is affected by many factors, such as the replacement ratio and quality of recycled coarse aggregate

(RCA) [14,15], the concrete cover [16,17], the diameter of steel reinforcement [18,19], the anchoring length [20], and the types of additives (such as fibers and polymers) [21–24].

RAC structures inevitably experience freeze–thaw cycles due to the cold climate in frigid regions, which leads to the deterioration of the physical and mechanical properties of RAC [25]. Consequently, the determination of the freeze–thaw resistance of RAC before the construction of RAC structures in frigid regions is necessary, and some research has aimed at evaluating the mechanical properties of RAC after freeze–thaw cycles and the freeze–thaw resistance of RAC [26–28]. The bond performance of steel reinforcement and RAC is also influenced by freeze–thaw cycles. Hence, several investigations have assessed the bond performance of steel reinforcement and RAC after freeze–thaw cycles using the pull-out test [29–36], which demonstrated that the bond strength decreases with the increase in freeze–thaw cycles, but there is disagreement about the relationship between the slip and the freeze–thaw cycles in these investigations. Most scholars think that the slip between steel reinforcement and RAC increases with the increase in freeze–thaw cycles [29–35], but Shang et al. [36] found that the slip at the free end of plain steel reinforcement decreased with the increase in freeze–thaw cycles in seawater before 25 freeze–thaw cycles, which was different from the test results of Ren et al. [32] and Su et al. [33–35] on RAC specimens after freeze–thaw cycles in a salt solution. In addition, the bond strength of steel reinforcement and RAC after freeze–thaw cycles was not only affected by the number of freeze–thaw cycles but also affected by the anchoring parameters. In the above investigations, both Jiang et al. [29] and Liu et al. [30] considered the effect of the replacement ratio of RCA; Liu et al. [30] thought the deterioration rate of the bond strength after freeze–thaw cycles accelerated as the replacement ratio of RCA increased, while Jiang et al. [29] found that the replacement ratio of RCA affected the bond strength slightly. This was because all specimens had the same cubic compressive strength due to a lower water/cement ratio and larger cement consumption, which reduced the effect of the replacement ratio of RCA on the bond strength. Both Shang et al. [31,36] and Ren et al. [32] studied the influence of the steel reinforcement diameter on bond strength after freeze–thaw cycles and revealed that the bond strength decreased as the steel reinforcement diameter increased, regardless of freeze–thaw cycles, which closely corroborated the test results of Cao et al. [37] in beam-type tests. Additionally, the test results of Cao et al. [37,38] and Wang et al. [39] demonstrated that the bond strength after freeze–thaw cycles decreased as the anchoring length increased.

The preceding research has focused on the bond performance of steel reinforcement and RAC after freeze–thaw cycles. Nevertheless, in a frigid marine environment, due to the cold climate and high concentration of chloride ions in the seawater, RAC structures not only experience freeze–thaw cycles but also experience steel reinforcement corrosion due to seawater. As is well-known, the cross-sectional area of the steel reinforcement was reduced with an increase in the steel reinforcement corrosion rate [40]; meanwhile, the steel reinforcement corrosion products, which had volume expandability, increased gradually with an increase in the steel reinforcement corrosion rate [41]. The mechanical properties of the steel reinforcement decreased due to a reduction in the cross-sectional area of the steel reinforcement, which led to the deterioration of the durability and bearing capacity of the structure [42,43]. The steel reinforcement corrosion products induced swelling stress on the concrete, which led to cracking and spalling of the concrete cover, and thus the bond performance decreased with a reduction in horizontal restraint provided by the concrete cover [44,45]. Therefore, the bond performance of corroded steel reinforcement and RAC needed to be studied adequately, and some scholars likewise conducted relevant investigations. Alhawat et al. [46,47] indicated that the bond performance increased slightly and then decreased pronouncedly with an increase in the steel reinforcement corrosion rate, which was in accord with the test results of Zhao et al. [13]. Additionally, Zhao et al. [13] observed that the tendency of the bond performance degeneration between RAC and natural aggregate concrete (NAC) structures was similar, and the difference in the bond performance between RAC and NAC structures could be decreased by the installation of

stirrups. The effects of the replacement ratio of RCA on the bond performance of corroded steel reinforcement and RAC were investigated, and Yang et al. [48] showed that the bond performance reduced as the replacement ratio of RCA increased, while the effects were slight. However, Fernandez et al. [49] presented a different opinion; they indicated that the effects of the replacement ratio of RCA on the bond performance of RAC structures with a 50% replacement ratio of RCA were slight, while the effects became great for RAC structures with a 100% replacement ratio of RCA.

The majority of the above research focused on the separate effect of steel reinforcement corrosion or freeze–thaw cycles on the bond performance of steel reinforcement and RAC, but little research has focused on the coupled effect of both two factors on bond performance. Some research has focused on the coupled effect of steel reinforcement corrosion and freeze–thaw cycles on the bond performance of steel reinforcement and NAC [50,51], and the test results demonstrate that bond performance was influenced by a superimposed damage effect. Liu et al. [50] proposed an empirical formula of the ultimate bond strength considering the stirrup corrosion rate, freeze–thaw cycles, and stirrup ratio and established a bond–slip prediction model considering the stirrup spacing, stirrup corrosion rate, and freeze–thaw cycles based on the eccentric pull-out test results. Zhang et al. [51] revealed that freeze–thaw cycles increased the pore structure damages of concrete and accelerated steel reinforcement corrosion based on microscopic tests and center pull-out tests and proposed a bond strength damage model considering the steel reinforcement corrosion rate and freeze–thaw cycles. However, both research studies focused on the bond performance of NAC structures under the coupled effect of steel reinforcement corrosion and freeze–thaw cycles and could not provide data supporting the investigation of the bond performance of RAC structures under the coupled effect of steel reinforcement corrosion and freeze–thaw cycles, and should therefore only be a reference for analysis.

The bond performance of RAC structures is necessarily affected by the coupled effect of steel reinforcement corrosion and freeze–thaw cycles in a frigid marine environment, but little research has focused on this topic. Therefore, the objective of this research was to investigate the bond performance of corroded steel reinforcement and RAC after freeze–thaw cycles using the center pull-out test and combining the evolution of mechanical properties parameters after freeze–thaw cycles (e.g., mass loss, cubic compressive strength, and dynamic elastic modulus loss). The relationships between the ultimate bond strength and different freeze–thaw cycles and steel reinforcement corrosion rates are presented through the relativity analysis, and the pull-out energy of RAC specimens with different steel reinforcement corrosion rates after freeze–thaw cycles is presented. Additionally, a modified bond–slip prediction model of corroded steel reinforcement and RAC after freeze–thaw cycles is established. This bond–slip prediction model's result was compared with other research, indicating its rationality and applicability. The test results provide new supporting data for the evaluation of freeze–thaw resistance and bond performance of RAC structures in a frigid marine environment.

2. Materials and Methods

The objective of the test program was to test the freeze–thaw resistance of RAC (NAC) and the bond performance of corroded steel reinforcement and RAC after freeze–thaw cycles and to investigate how steel reinforcement corrosion and freeze–thaw cycles affected the bond strength of RAC specimens. Therefore, serial tests were carried out. The test procedure included the electrochemical corrosion test, the rapid freeze–thaw cycle test, material properties tests, and the pull-out test. The parameters tested included the mass, the cubic compressive strength, the dynamic elastic modulus, the ultimate bond strength, and the bond–slip. The test procedure is plotted in Figure 1.

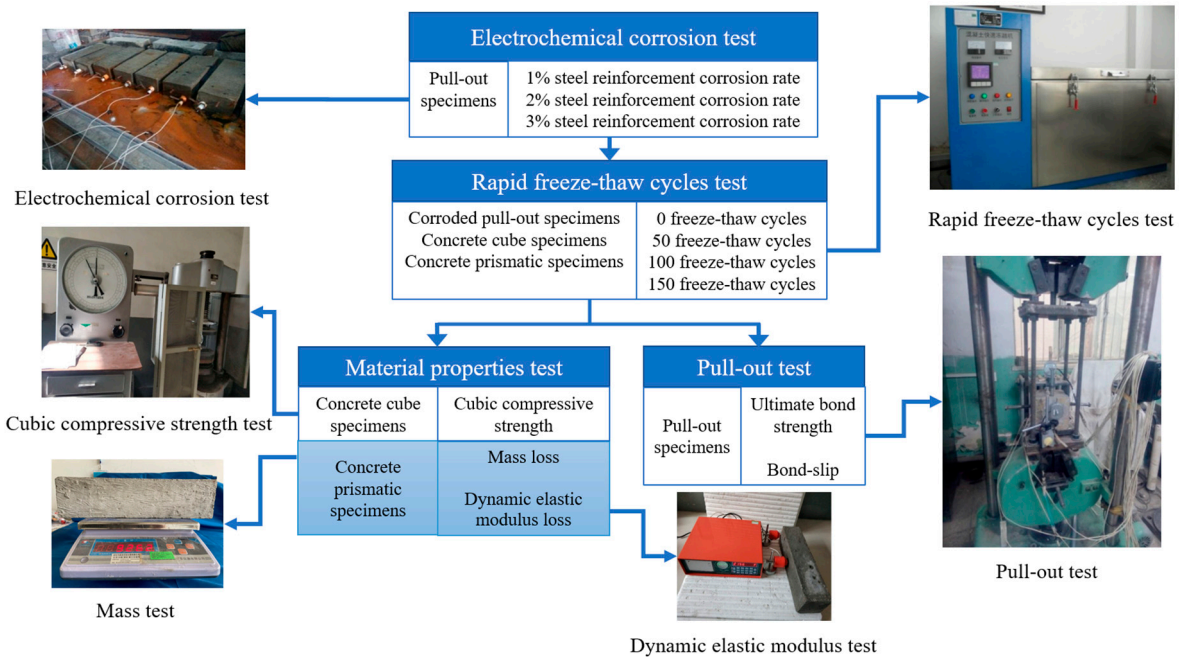


Figure 1. Flow chart of the test.

2.1. Materials and Mixture Proportions

Ordinary Portland cement of strength grade 42.5, which complied with China specification GB175-2007 [52], was employed as cement-based material, and the cement properties are tabulated in Table 1. Natural river sand was employed as a fine aggregate, and the fine aggregate properties are tabulated in Table 2. Natural crushed stone was employed as a natural coarse aggregate (NCA). After crushing and screening waste concrete from a demolished factory in Baotou, the recycled crushed stone was prepared and employed as RCA (a photo of RCA is shown in Figure 2). The original cubic compressive strength of the waste concrete was 45.5 MPa. The gradation curve of RCA and NCA is plotted in Figure 3, and the physical properties of RCA and NCA are tabulated in Table 3. A GL-B4-efficient, air-entraining, water-reducing agent, which complied with China specification GB 8076-2008 [53], was added per concrete mixture to achieve a minimum air content of 5%.

Table 1. Cement properties.

Property			Value
Type and Class			P.O 42.5
Density (g cm^{-3})			3.10
Fineness (%)			4.5
Setting times (min)	Initial setting times		118
	Final setting times		224
Stability			Qualified (No bending and crack)
Strength (MPa)	Compressive strength	3 day	25.5
		28 day	47.9
	Flexural strength	3 day	4.1
		28 day	7.5

The deformed steel reinforcement with a nominal yield strength of 400 MPa and a diameter of 16 mm was employed as steel reinforcement, while the deformed steel

reinforcement with a nominal yield strength of 335 MPa and a diameter of 8 mm was employed as stirrups [54]. The steel reinforcement properties are tabulated in Table 4.

Table 2. Fine aggregate properties.

Property	Value
Fineness Module	2.5
Mud Content (%)	2.8
Apparent density (g cm^{-3})	2.65



Figure 2. Photo of RCA.

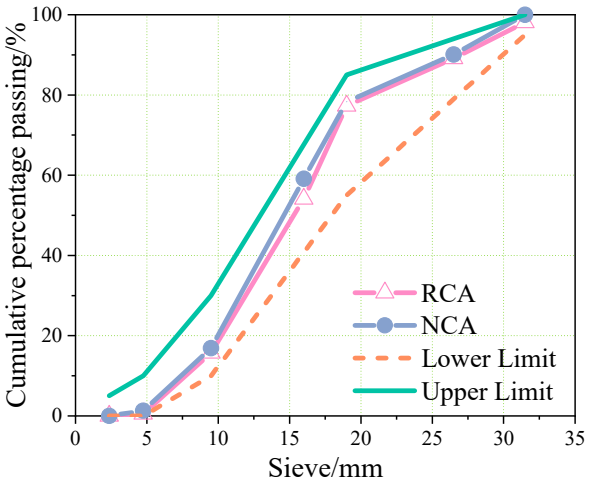


Figure 3. Gradation curves of NCA and RCA.

Table 3. Physical properties of NCA and RCA.

Property	Type	
	NCA	RCA
Size of particles (mm)	5–31.5	5–31.5
Apparent density (kg m^{-3})	2812	2597
Bulk density (kg m^{-3})	1478	1211
Content of needle-like particle (%)	1.2	8.2
Mud content (%)	1.3	5.5
Crushing index (%)	10.2	16.5
Water absorption of 10 min (%)	0.5	2.3
Water absorption of 1 day (%)	1.1	5.6

Table 4. Steel reinforcement properties.

Property	Type	
	HRB400	**HRB335**
Diameter d (mm)	16	8
Tensile strength f_t (MPa)	550	460
Yield strength f_y (MPa)	410	340
Modulus of elasticity E_s (MPa)	2.01×10^5	2.03×10^5

RCA was pre-wetted, with the added water reaching a saturated surface-dry state (SSD) to ensure good workability of RAC due to the water absorption of RCA being nearly 5 times higher than that of NCA according to the measured results and the amount of added water confirmed according to the measured results of the 10 min water absorption of RCA [34]. The amount of water in RAC did not include pre-added water. Two mixtures were selected and cast to assess the mechanical properties of RAC and NAC, and the mixture proportions are tabulated in Table 5. The concrete specimens were placed in fresh water for 28 days to cure, while the pull-out specimens were cured in a NaCl solution with a 5% concentration for 4 days after 24 days of curing in fresh water to ensure that the specimens were permeated well by chloride. The 28-day compressive strength of NAC and RAC was measured at 36.8 MPa and 35.5 MPa, respectively. The measured air content of NAC and RAC was 5.6% and 5.4%, respectively.

Table 5. Mixture proportions.

Property	Type	
	NAC	**RAC**
Replacement ratio of RCA (%)	0	100
Water/cement ratio	0.5	0.5
Cement (kg m^{-3})	320	320
Water (kg m^{-3})	160	160
Coarse aggregate (kg m^{-3})	1129	1110
Sand (kg m^{-3})	820	820
Concrete admixture (kg m^{-3})	8.32	8.32

2.2. Specimen Preparation

The steel reinforcements were separately cast in the interior of 12 concrete cube specimens with side lengths of 150 mm to conduct the center pull-out tests according to China specification GB/T50152-2012 [55], and the reinforcement layout and schematic diagram of the pull-out specimen are shown in Figure 4. The stirrup spacing was set as 50 mm [33,54], and the reinforcement ratio of the pull-out specimens was 0.02. Additionally, the anchoring length of the steel reinforcement and the concrete was designed as 80 mm, 5 times the diameter of the steel reinforcement, to guarantee a uniform distribution for the bond stress and a diminution of local extrusion stress on the load end. Beyond the pale of the anchoring length, the steel reinforcement was covered with two PVC pipes to achieve an accurate anchoring length. Paraffin wax was employed to seal the void between the PVC pipe and the steel reinforcement to prevent the inflow of cement mortar. Notably, the 5% NaCl solution was employed in the concrete mix of pull-out specimens rather than fresh water to enhance the chloride ion concentration in the interior of the concrete and ensure the accuracy of the steel reinforcement corrosion rate.

Additionally, 24 concrete cube specimens with side lengths of 150 mm were cast to conduct a contrast test on the cubic compressive strength of NAC and RAC after freeze–thaw cycles; 6 concrete prismatic specimens with sizes of 100 mm × 100 mm × 400 mm were cast to conduct a contrast test on the mass loss and the dynamic elastic modulus loss of NAC and RAC after freeze–thaw cycles. The concrete cube and prismatic specimens

were cast according to China specification GB/T 50081-2019 [56]; measurement of the cubic compressive strength was performed according to China specification GB/T 50081-2019 [56]; measurements of the mass loss and the dynamic elastic modulus loss were carried out according to China specification GB/T 50082-2009 [57].

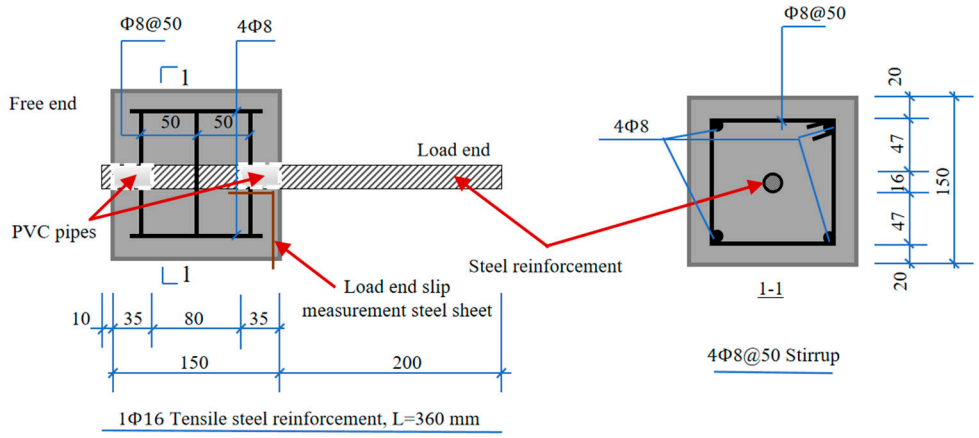


Figure 4. Schematic diagram of pull-out specimen.

2.3. Electrochemical Corrosion Test and Rapid Freeze–Thaw Cycle Test

The process of steel reinforcement corrosion is long and slow in the natural environment, while the electrochemical accelerated method was employed to supersede natural corrosion, which can achieve similar corrosion damage rather quickly [58]. Based on the study of Wang et al. [59], the electrochemical corrosion test was performed, and 0.02 mA/mm^2 was employed as the current density in the electrochemical corrosion test. Specimens with steel reinforcement were soaked in the 5% NaCl solution, and the NaCl solution level was about 10 mm lower than the bottom surface of the steel reinforcement. The steel reinforcement was connected to the anode of the HYL-A constant direct current supply, while the copper sheet immersed in the NaCl solution was connected to the cathode of the HYL-A constant direct current supply. The schematic diagram of the electrochemical corrosion test setup is shown in Figure 5. A total of 3 targeted steel reinforcement corrosion rates (1%, 2%, and 3%) of the corrosion specimens were obtained by controlling the contact time between the specimens and the impressed current; the contact time can be estimated in terms of Faraday's law of electrolysis, as shown in Equation (1).

$$t = \frac{2\eta Nme}{MI} \tag{1}$$

where t is the theoretical corrosion time; η is the targeted steel reinforcement corrosion rate; M is the molar mass of steel reinforcement, 56 g mol^{-1}; I is the average current; N is the avogadro constant, 6.02 × 10^{23} mol^{-1}; m is the initial mass of the steel reinforcement; e is the electron charge, 1.6 × 10^{-19} C.

After the electrochemical corrosion tests, rapid freeze–thaw cycle tests were conducted according to the China specification GB/T 50082-2009 [57] in the IMDR-16 rapid freeze–thaw testing machine with the quick-freeze method to investigate the freeze–thaw resistance of concrete specimens and the pull-out specimens. The specimens were immersed in fresh water during the rapid freeze–thaw cycle test, and the level of fresh water was 5 mm higher than the upper surface of the specimens. Additionally, the temperature of the specimens was controlled to range from +8 ± 2 °C to −17 ± 2 °C during every freeze–thaw cycle, and the duration of each freeze–thaw cycle was 3.5 h. The mass and the dynamic elastic modulus of prismatic concrete specimens and the cubic compressive strengths of concrete cube specimens after every 50 freeze–thaw cycles were measured, and these were stopped after 150 freeze–thaw cycles.

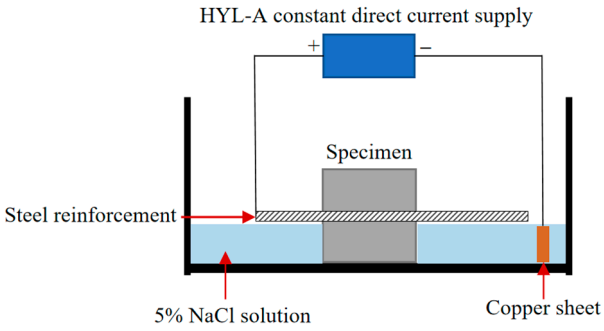


Figure 5. Schematic diagram of electrochemical corrosion test setup.

2.4. Pull-Out Test

After the rapid freeze–thaw cycle test, the pull-out tests were conducted in a 600 kN hydraulic servo testing machine to obtain the bond strengths and the bond–slip curves according to the China specification GB/T 50152-2012 [55]. A schematic diagram of the pull-out test setup is plotted in Figure 6. A load sensor was used to monitor the applied load, and one displacement sensor was installed at the free end of the steel reinforcement and the hard steel sheet, which was welded with the load end of the steel reinforcement, respectively, to monitor the slips. The test data were gathered with a static data acquisition system. Two control methods were employed to control the loading rates of the applied force, including the load-control method and the displacement-control method. Before the applied speed exceeded 0.80 P_u (P_u is the ultimate pull-out force of the pull-out tests), the load-control method was employed, and the loading speed loaded on the pull-out specimens was 0.1 kN/s. Then, the displacement-control method was employed after the applied force exceeded 0.80 P_u and the loading speed reached 0.3 mm/min.

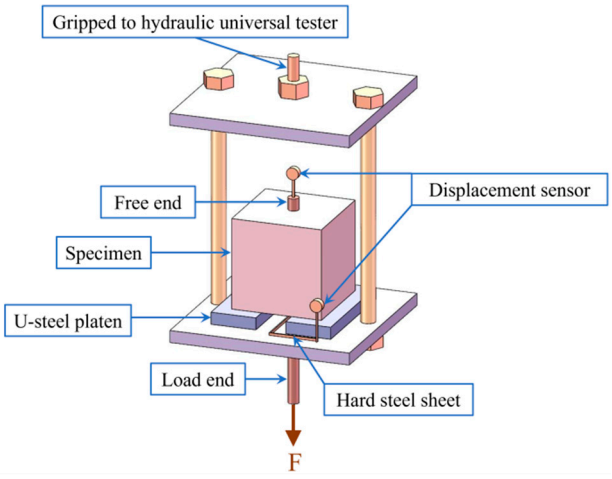


Figure 6. Schematic diagram of pull-out test setup.

According to the pull-out forces and the slips monitored and gathered, the bond strength and the slip of steel reinforcement and concrete were calculated with Equations (2) and (3), respectively.

$$\tau = \frac{P}{\pi d l} \tag{2}$$

$$s = \frac{s_l + s_f}{2} \tag{3}$$

where τ is the average bond strength; P is the pull-out force; d is the diameter of the steel reinforcement; l is the anchoring length; s is the average slip; s_l is the slip at the load end; s_f is the slip at the free end.

3. Results and Analysis

3.1. Corrosion Performance of the Steel Reinforcement Embedded in RAC

In the early stages of the process of the corrosion test, lots of tiny bubbles got away from the copper sheet, and then a stratum of bronze bubbles existed at the surface of the NaCl solution. Subsequently, the steel reinforcement corrosion products located in the anchoring interfaces between the steel reinforcement and the concrete were produced, and the color of the steel reinforcement corrosion products changed from dark green to reddish-brown. This is because at the early stages of the process of the corrosion test, due to a lack of oxygen, the steel reinforcement corrosion products occur incomplete oxidation leading to the dark green color of steel reinforcement corrosion products. However, a complete oxidation reaction of the steel reinforcement corrosion products is achieved later, resulting in the reddish-brown color of steel reinforcement corrosion products [60].

The corrosion specimens were divided into two sections after the pull-out test, and then the corroded steel reinforcement was removed and treated. Treatment of the corroded steel reinforcements included cleaning with dilute hydrochloric acid, acid neutralization with alkali, and rinsing with fresh water. Finally, the steel reinforcements were dried and weighed. Each corroded steel reinforcement and two non-corroded steel reinforcements of the same kind as the corroded steel reinforcement were treated together after the same freeze–thaw cycles to avoid the effects of the treatment on the measurement of the corrosion rate. The corrosion rate of the corroded steel reinforcements can be calculated using Equation (4) according to the China specification JTS/T 236-2019 [61].

$$\eta = \frac{m_0 - m - \frac{(m_{01} - m_1) + (m_{02} - m_2)}{2}}{m_0} \times 100\% \quad (4)$$

where η is the actual steel reinforcement corrosion rate; m_{01} and m_{02} are the mass of two non-corroded steel reinforcements before the treatment, respectively; m_1 and m_2 are the mass of two non-corroded steel reinforcements after the treatment, respectively; m_0 is the initial mass of the corroded steel reinforcement; m is the mass of the corroded steel reinforcement after the treatment.

The appearances of corroded steel reinforcements after the treatment are plotted in Figure 7. It could be observed that the quantity and depth of corrosion pits and the corrosion degree of steel reinforcements with a higher steel reinforcement corrosion rate were more pronounced compared to that with a low steel reinforcement corrosion rate.

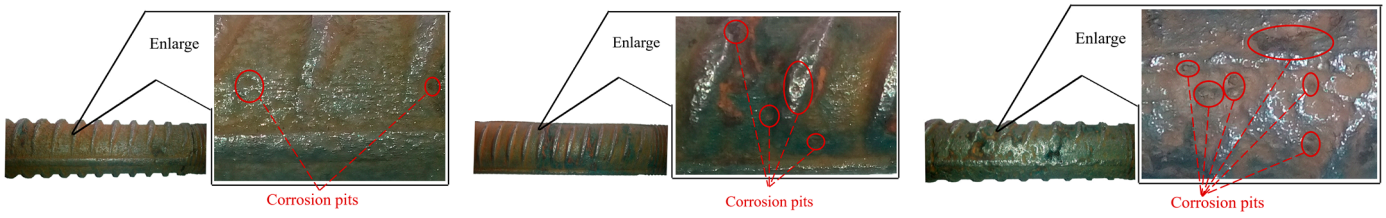


Figure 7. Appearances of corroded steel reinforcements. (**a**) 1% steel reinforcement corrosion rate. (**b**) 2% steel reinforcement corrosion rate. (**c**) 3% steel reinforcement corrosion rate.

A comparison of actual and target steel reinforcement corrosion rates is tabulated in Table 6, and the difference between actual and target steel reinforcement corrosion rates of most steel reinforcements was small, while some actual steel reinforcement corrosion rate was slightly higher than the target steel reinforcement corrosion rate with increasing freeze–thaw cycles, which can be explained by the enhancing effect of freeze–thaw cycles on the deterioration of steel reinforcement corrosion.

Table 6. Comparison of actual and target steel reinforcement corrosion rate.

Specimen	Initial Mass (g)	Mass of Corroded Steel Reinforcement after Treatment (g)	Mass Loss (g)	Actual Steel Reinforcement Corrosion Rate (%)	Target Steel Reinforcement Corrosion Rate (%)
RC0-0	235.12	235.12	0	0	0
RC1-0	238.52	236.30	2.21	0.93	1
RC2-0	240.51	235.45	5.05	2.10	2
RC3-0	246.14	238.24	7.90	3.19	3
RC0-50	238.32	238.32	0	0	0
RC1-50	236.54	234.48	2.05	0.97	1
RC2-50	239.12	233.86	5.26	2.19	2
RC3-50	240.20	232.48	7.72	3.21	3
RC0-100	234.51	234.51	0	0	0
RC1-100	237.23	234.11	3.08	1.30	1
RC2-100	250.30	244.64	5.65	2.26	2
RC3-100	242.80	234.90	7.90	3.25	3
RC0-150	238	238	0	0	0
RC1-150	237.20	234.70	2.49	1.05	1
RC2-150	235.00	229.75	5.24	2.23	2
RC3-150	242.23	234.23	7.99	3.30	3

3.2. Freeze–Thaw Resistance of the Concrete

3.2.1. Appearances of Pull-Out Specimens after Freeze–Thaw Cycles

The appearance of the concrete specimens with a 1% steel reinforcement corrosion rate after freeze–thaw cycles is shown in Figure 8. The surface of specimens showed slight spallation after 50 freeze–thaw cycles. Half of the RAC specimens showed the exposure and spallation of RCA after 100 freeze–thaw cycles and obtained a rougher surface. Coarse aggregate exposure and more severe aggregate spallation occurred on the surfaces of all specimens after 150 freeze–thaw cycles and the corners of 70% of the specimens were damaged.

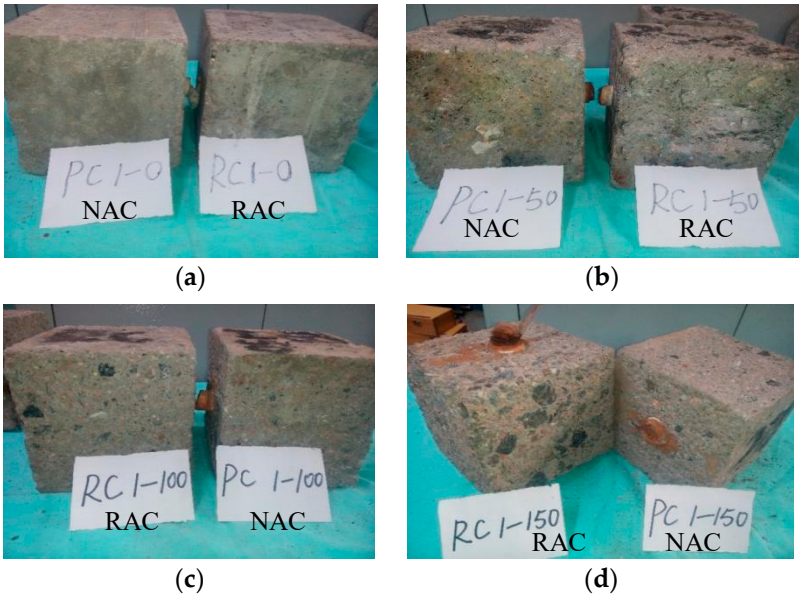


Figure 8. Appearances of RAC and NAC after freeze–thaw cycles. (**a**) 0 freeze–thaw cycle. (**b**) 50 freeze–thaw cycles. (**c**) 100 freeze–thaw cycles. (**d**) 150 freeze–thaw cycles.

The surface damage of RAC specimens was more severe than that of NAC specimens after the same freeze–thaw cycles, which revealed that the freeze–thaw resistance of RAC was inferior to that of NAC. Su et al. [33] and Li et al. [12] also came to similar conclusions. The reason is that the amount of the interfacial transition zone (ITZ) in the interior of

RAC is larger, and the ITZ is weaker and more easily damaged by freeze–thaw cycles [27]. Additionally, the quantity of infiltrating water was larger in RAC compared to that in NAC after fewer freeze–thaw cycles due to the higher porosity of RAC, which leads to faster damage to RAC.

3.2.2. Mass Loss

The mass loss, the cubic compressive strength, and the dynamic elastic modulus loss of the concrete specimens after freeze–thaw cycles were measured to assess the freeze–thaw resistance of the concrete (RAC and NAC).

The mass of concrete specimens initially increased and subsequently decreased with increasing freeze–thaw cycles, which was similar to the conclusions reached by Liu et al. [26], Wu et al. [27], and Su et al. [33]. This can be explained by the combined effects of water infiltrates and cement mortar spalling on the mass of the concrete. Water infiltrates the concrete with increasing freeze–thaw cycles due to the disruption of the pore structure by the freeze–thaw stress, which contributes to the concrete hydration and aggregate water absorption, increasing the concrete mass. In addition, the freeze–thaw stress caused by the repeated freezing and thawing of the infiltrating water causes cracking in the interior of the concrete. The quantity and size of these cracks constantly increase with increasing freeze–thaw cycles, causing the cement mortar to loosen and spall, which leads to a reduction in the mass of the concrete. The mass of the specimens increases from 0 to 50 freeze–thaw cycles because the mass of the infiltrating water is greater compared to that of the cement mortar spalling, while the mass of the specimens decreases after 100 freeze–thaw cycles because the mass of the infiltrating water is less than that of the cement mortar spalling.

Figure 9 demonstrates that the mass loss of RAC was more influenced by freeze–thaw cycles than that of NAC; the mass increase of RAC after 50 freeze–thaw cycles was 1.8 times that of NAC, while the mass loss of RAC after 150 freeze–thaw cycles was 1.2 times that of NAC. This can be explained by the inferior freeze–thaw resistance of RAC to that of NAC.

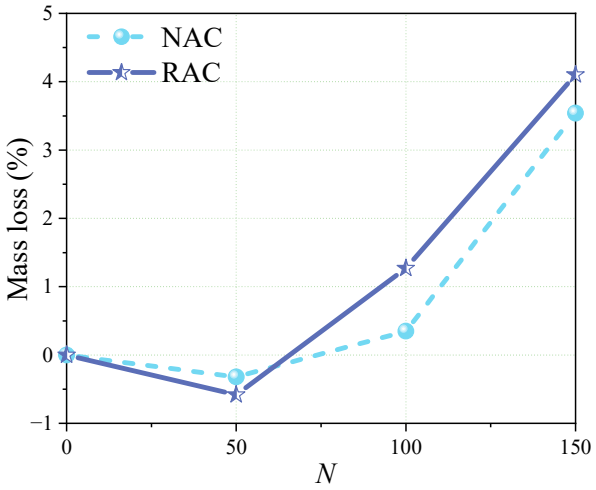


Figure 9. Mass loss of RAC and NAC.

3.2.3. Cubic Compressive Strength

The cubic compressive strength of RAC and NAC after different freeze–thaw cycles is shown in Figure 10, and the cubic compressive strength followed an almost straight-line downward tendency with increasing freeze–thaw cycles. The cubic compressive strength loss of RAC (NAC) after every 50 freeze–thaw cycles was close to 17.05% (14.93%), which is similar to the test results of Wu et al. [27]. This is because the quantity of deleterious pores and cracks increases due to the repeated freeze–thaw stress, which causes a large decrease in the cubic compressive strength of concrete [62].

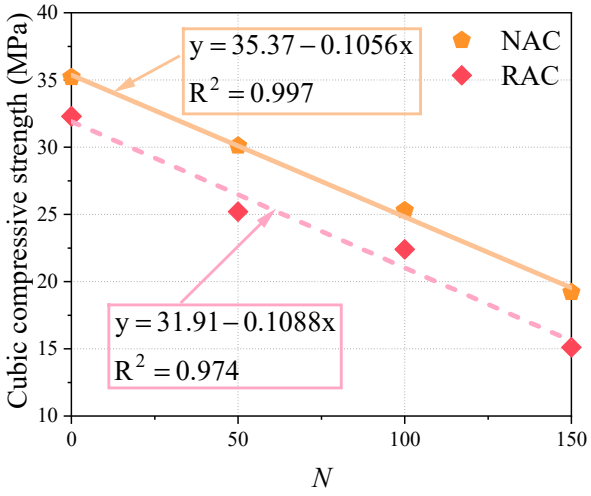


Figure 10. Cubic compressive strength of RAC and NAC.

Figure 10 reveals that the cubic compressive strength of RAC was less than that of NAC before freeze–thaw cycles with the same water–cement ratio, and the initial cubic compressive strength of RAC (NAC) was 32.3 MPa (35.2 MPa). This can be explained by the incomplete hydration of the cement due to high water absorption and more defects in RCA, leading to a low cubic compressive strength of RAC. Additionally, the cubic compressive strength of RAC decreased slightly faster after freeze–thaw cycles compared to that of NAC in terms of the comparison of the slopes of the fitting curves between the cubic compressive strength after freeze–thaw cycles of RAC and NAC. This is because the lower initial cubic compressive strength of RAC means that the compactness of RAC is poorer than that of NAC, which leads to poorer freeze–thaw resistance of RAC compared to that of NAC. Therefore, the cubic compressive strength deterioration after freeze–thaw cycles of RAC is more rapid than that of NAC.

3.2.4. Dynamic Elastic Modulus Loss

The dynamic elastic modulus loss is calculated by Equation (5) based on the measured results of the dynamic elastic modulus of the concrete (RAC and NAC) after freeze–thaw cycles.

$$\Delta E(N) = \frac{E_0 - E_N}{E_0} \times 100\% \quad (5)$$

where $\Delta E(N)$ is the dynamic elastic modulus loss after N freeze–thaw cycles; E_0 is the dynamic elastic modulus before freeze–thaw cycles; E_N is the dynamic elastic modulus after N freeze–thaw cycles.

The dynamic elastic modulus is tabulated in Table 7, and the dynamic elastic modulus loss is displayed in Figure 11. The dynamic elastic modulus loss of RAC and NAC gradually increased with increasing freeze–thaw cycles, and the dynamic elastic modulus loss after 150 freeze–thaw cycles of RAC (NAC) reached 42.8% (33.5%).

Table 7. Dynamic elastic modulus of RAC and NAC after freeze–thaw cycles.

	Freeze–Thaw Cycles	Type	
		NAC	RAC
Dynamic Elastic Modulus (MPa)	0	30.6	29.25
	50	27.35	24.72
	100	25.21	19.15
	150	20.33	16.72

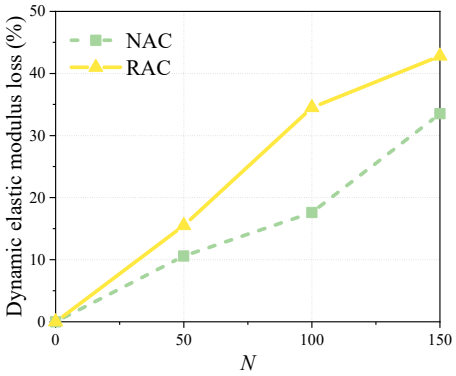


Figure 11. Dynamic elastic modulus loss of RAC and NAC.

Furthermore, the dynamic elastic modulus loss of RAC increased more rapidly than that of NAC from 0 to 100 freeze–thaw cycles, while the dynamic elastic modulus loss of RAC increased more slowly than that of NAC after 100 freeze–thaw cycles. The reason for this is that the concrete completeness of NAC is severely destroyed after 100 freeze–thaw cycles, resulting in a rapid increase in the dynamic elastic modulus loss. Due to the crack-free cement paste of NAC before 100 freeze–thaw cycles, the concrete completeness of NAC is better than that of RAC, which leads to less freeze–thaw damage [12]. However, cracks not only exist at the interface between the cement paste and NCA but also appear in the interior of the cement paste of NAC after 100 freeze–thaw cycles, which causes poorer concrete completeness of NAC and more severe freeze–thaw damage to NAC than that to RAC. Therefore, the increase in the dynamic elastic modulus loss of NAC becomes more rapid compared to that of RAC after 100 freeze–thaw cycles.

The cubic compressive strength and the dynamic elastic modulus loss of RAC and NAC after freeze–thaw cycles are displayed in Figure 12. Figure 12 shows the cubic compressive strength deceased as the dynamic elastic modulus loss increased, which demonstrates an increase in damage for concrete causes a decrease in cubic compressive strength of RAC and NAC after freeze–thaw cycles.

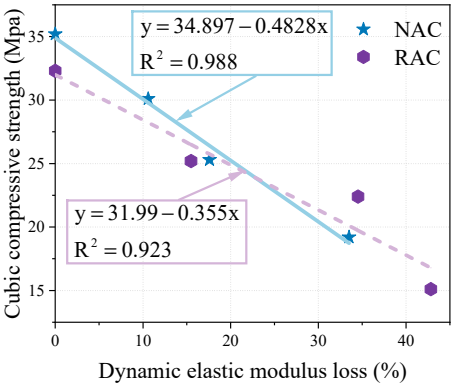


Figure 12. Cubic compressive strength and dynamic elastic modulus loss.

3.3. Failure Pattern of Pull-Out Specimen

Figure 13 shows the failure pattern of the pull-out specimens, and the failure patterns of all specimens were pull-out failures. The coupled effect of freeze–thaw cycles and steel reinforcement corrosion did not alter the failure pattern, and the difference in the failure pattern between RAC and NAC was minimal. All pull-out specimens with stirrups exhibited the same failure pattern, the pull-out of the embedded steel reinforcement from the concrete, which was identical to the test result of Su et al. [33]. This can be explained by the cracking of the concrete prevented by the lateral restraint contributed by the stirrups.



Figure 13. Failure pattern of pull-out specimen.

3.4. Ultimate Bond Strength

The ultimate bond strength of corroded steel reinforcement and RAC after freeze–thaw cycles are plotted in Figure 14, and the ultimate bond strength of RAC specimens with a 0% corrosion rate of the previous study by Su et al. [33] after freeze–thaw cycles was used as a reference to investigate the coupled effect of freeze–thaw cycles and steel reinforcement corrosion on the ultimate bond strength.

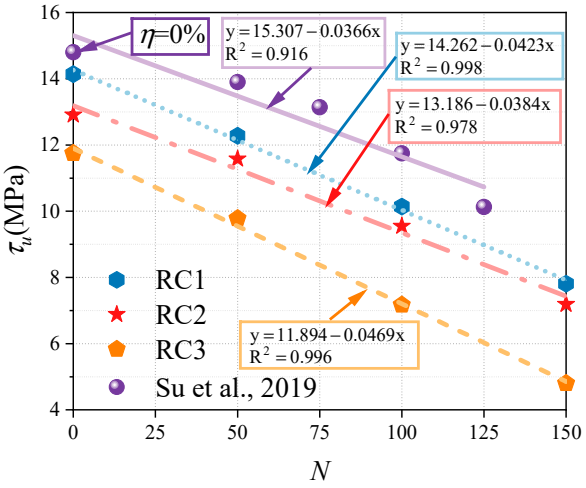


Figure 14. Ultimate bond strength measured by this study and Su et al. [33].

Figure 14 shows that the ultimate bond strength reduced with increasing freeze–thaw cycles, indicating the deterioration of the bond performance of RAC specimens after freeze–thaw cycles. This is because the pore structure is destroyed by the freeze–thaw stress caused by the repeated freezing and thawing of the infiltrating water, and then the emergence and expansion of the cracks destroy the horizontal restraint provided by the concrete cover, which causes the ultimate bond strength to reduce. The cracks then extend to the interface of steel reinforcement and RAC with increasing freeze–thaw cycles, resulting in a reduction in the chemical adhesion and friction of steel reinforcement and RAC. The freeze–thaw cracks interact with the pull-out cracks, which causes a more severe reduction in the ultimate bond strength [26].

Moreover, the ultimate bond strength decreased with an increase in the steel reinforcement corrosion rate. The ultimate bond strength of RAC specimens with 0%, 1%, 2%, and 3% steel reinforcement corrosion rates was reduced by 4.46%, 12.77%, and 20.61%, respectively, before freeze–thaw cycles, compared with RAC specimens with a 0% corrosion rate. The mass loss of steel reinforcement and deposition of steel reinforcement corrosion products at the interface between steel reinforcement and RAC are caused due to steel reinforcement corrosion. The steel reinforcement corrosion products, which have volume

expansibility, induce hoop stress in the interior of the concrete. The concrete cover cracks due to the hoop stress, causing a reduction in the horizontal restraint provided by the concrete cover. On the other hand, the cracking of the concrete also can also induce a reduction in chemical adhesion and friction. Localized pitting corrosion and rib damage of the steel reinforcement are induced when the steel reinforcement corrosion rates arrive at a high level, leading to a deterioration of the interlocking between steel reinforcement and RAC.

Linear regression was performed on the ultimate bond strength of RAC specimens with different steel reinforcement corrosion rates after freeze–thaw cycles in Figure 14. The ultimate bond strength after freeze–thaw cycles with a 3% steel reinforcement corrosion rate decreased most rapidly, which means that the ultimate bond strength under the coupled effect of freeze–thaw cycles and steel reinforcement corrosion decreased more rapidly than that under separate effects. This is because the interaction of the corrosion-induced crack and the freeze–thaw cracks accelerates the deterioration of the ultimate bond strength.

3.5. Relativity Analysis

Relativity indicates the direction and degree between two related variables, and Pearson's product–moment relative coefficient is a practical application of relativity in concrete research [63]. Pearson's product–moment relative coefficient was employed in this analysis to assess the relationships between the ultimate bond strength and different freeze–thaw cycles and steel reinforcement corrosion rates, expressed as Equation (6), and the assessment results are tabulated in Table 8.

$$r = \frac{\sum[(x-\overline{x})(y-\overline{y})]}{\sqrt{\sum\left[(x-\overline{x})^2\right]}\sqrt{\sum\left[(y-\overline{y})^2\right]}} \quad (6)$$

where r is the Pearson's relative coefficient; x and y are independent values; and $\overline{x}$ and $\overline{y}$ are average values of x and y, respectively. The range of r is -1 to $+1$, and y is positively related to x when r is a non-zero positive number; meanwhile, y is negatively related to x when r is a non-zero negative number.

Table 8. Assessment results of the relative coefficient.

	Freeze–Thaw Cycles	Steel Reinforcement Corrosion Rates	Ultimate Bond Strength
Freeze–thaw cycles	1	0	−0.9988
Steel reinforcement corrosion rates	0	1	−0.7872
Ultimate bond strength	−0.9988	−0.7872	1

The assessment results in Table 8 show the strong negative relativity between the ultimate bond strength and the freeze–thaw cycles and the steel reinforcement corrosion rates, with relative coefficients of −0.9988 and −0.7872, respectively. The relative coefficient between the freeze–thaw cycles and the steel reinforcement corrosion rates was zero, meaning no relativity. A comparison of these relative coefficients was made, demonstrating that the effect of freeze–thaw cycles on the ultimate bond strength is more pronounced compared to that of the steel reinforcement corrosion rates.

3.6. Bond–Slip Curve

The bond–slip curves are depicted in Figure 15, which proposes the variation law of the same steel reinforcement corrosion rate after different freeze–thaw cycles. The bond–slip curves were compared and found to be similar to the tendency for the typical bond–slip curve plotted in Figure 16, where τ_1, τ_u, s_u, and τ_r are the initial bond strength, ultimate

bond strength, peak slip, and residual bond strength, respectively. The bond–slip curves can be divided into four sections: the micro-slip section (OA), the slip section (AB), the descent section (BC), and the residual section (CD).

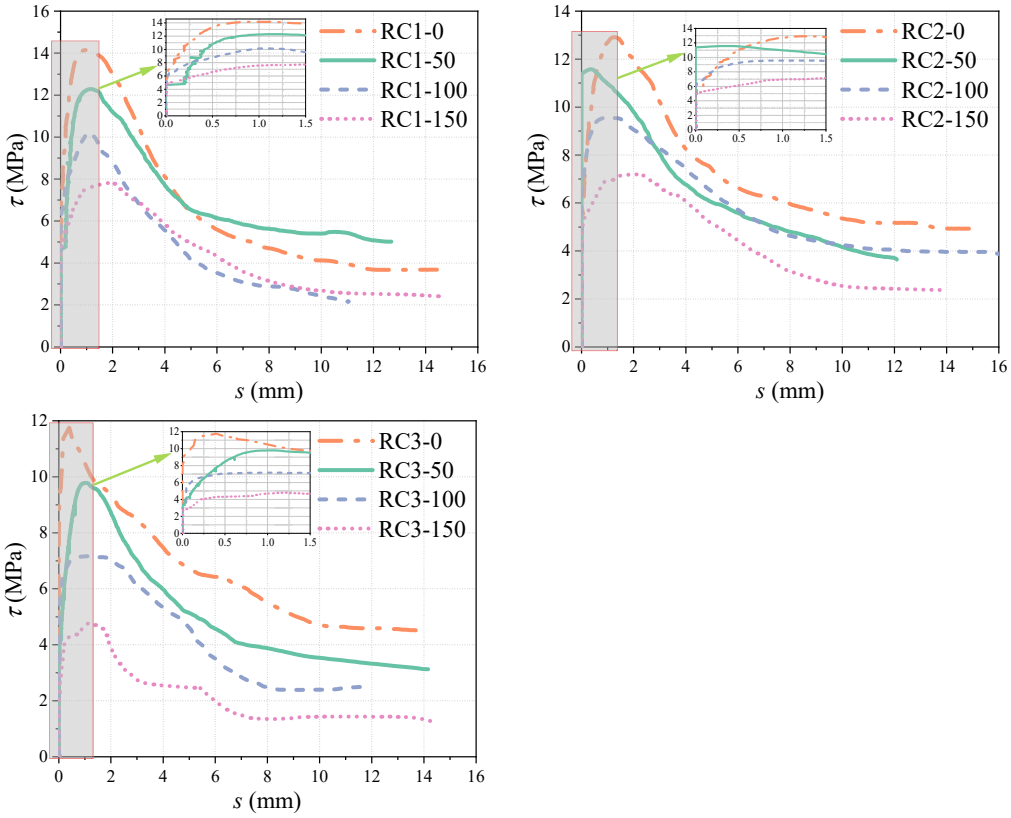


Figure 15. Average bond–slip curves of concrete specimens in the pull-out test.

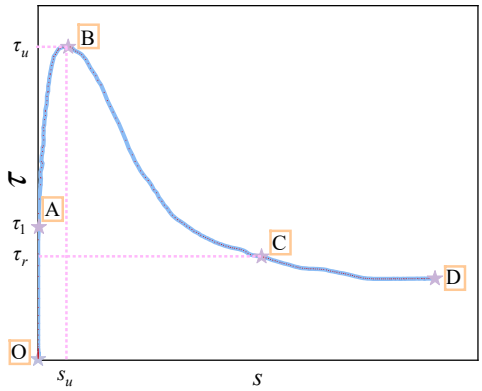


Figure 16. Typical bond–slip curve for concrete (O is original point at curve; A is the junction of micro-slip and slip sections at curve; B is the junction of slip and descent sections at curve; C is the junction of descent and residual sections at curve; D is the end at curve).

The micro-slip section (OA): the micro-slip section was a steep ascent until the bond strength reached the initial bond strength, and the bond strength was approximately linear, increasing up to about 0.34–0.98 of the ultimate bond strength, as illustrated in Figure 15. During this section, the bond strength experienced very rapid growth while the slip increase was negligible, and the bond strength was supplied by the static friction and chemical adhesion between RAC and deformed steel reinforcement.

The slip section (AB): as the pull-out force increased, the steel reinforcement would start to slip, and the static friction changed to dynamic friction. Moreover, chemical

adhesion was gradually lost, and interlocking began to play an essential role in the balance of the pull-out force until the ultimate bond strength was reached. This phenomenon was the same for all specimens with different corrosion rates until reaching 50 freeze–thaw cycles. However, the interlocking reduced pronouncedly after 100 freeze–thaw cycles, which led to a marked reduction in the slope of the slip section and the ultimate bond strength after 100 freeze–thaw cycles. This phenomenon can be explained by the occurrence of brittle damage in the concrete after 100 freeze–thaw cycles, which severely damages the bond of the steel reinforcement and the concrete, resulting in a rapid reduction in the ultimate bond strength after 100 freeze–thaw cycles.

The descent section (BC): the bond strength failed to maintain a relatively stable value after the pull-out force arrived at the value of the ultimate bond strength and began a rapid decline. In this section, the pull-out force was still balanced by dynamic friction and interlocking. However, due to the crushed mortar between the steel reinforcement ribs and the development of cracks in the RCA surface and cement matrix, the interlocking rapidly decreased, resulting in a rapid deterioration of the bond strength.

The residual section (CD): the bond–slip curve followed an approximately horizontal line when the bond strength exceeded a critical value, the residual bond strength. The pull-out force was balanced mainly by dynamic friction due to the pronounced reduction in interlocking. The range of residual bond strength was 0.21 to 0.41 times the ultimate bond strength.

3.7. Pull-Out Energy Analysis

The energy consumption of the pull-out force was obtained by calculating the area under the pull-out force–slip curves from its origin to the peak, and that can be referred to as the pull-out energy. The pull-out energy of RAC specimens with 1%, 2%, and 3% steel reinforcement corrosion rates is depicted in Figure 17. Moreover, based on the test data of Cao [54], the pull-out energy of RAC specimens with a 0% steel reinforcement corrosion rate after freeze–thaw cycles was calculated and used as a reference. The pull-out energy decreased with increasing freeze–thaw cycles for all steel reinforcement corrosion rates, and the pull-out energy loss with 0%, 1%, 2%, and 3% steel reinforcement corrosion rates was 16.97%, 23.11%, 15.63%, and 12.22%, respectively, after 100 freeze–thaw cycles. Moreover, the pull-out energy reduced with an increase in the steel reinforcement corrosion rate after the same number of freeze–thaw cycles, which is consistent with the tendency of variation in the bond strength shown in Figure 14. Compared to the pull-out energy with a 0% steel reinforcement corrosion rate, the pull-out energy was reduced by 6.45–26.18% with an increase in the steel reinforcement corrosion rate from 1% to 3% after 0 freeze–thaw cycles and the pull-out energy was reduced by 12.62–21.46% after 100 freeze–thaw cycles. The RAC surrounding the steel reinforcement hardened and became brittle due to steel reinforcement corrosion.

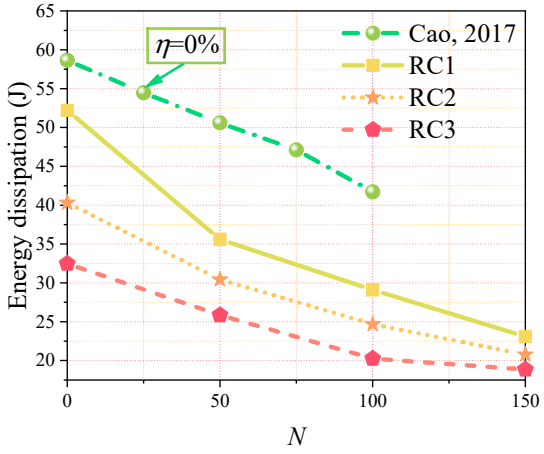


Figure 17. Pull-out energy measured by this study and Cao [54].

3.8. Bond–Slip Prediction Model under Coupled Effect of Freeze–Thaw Cycles and Steel Reinforcement Corrosion

A bond–slip prediction model under the coupled effect of freeze–thaw cycles and steel reinforcement corrosion is required to assess the bond–slip performance of RAC structures in a frigid marine environment. For more convenient modeling, normalization of bond strength and slip was performed and the normalized bond–slip ($\tau/\tau_u - s/s_u$) curves are displayed in Figure 18.

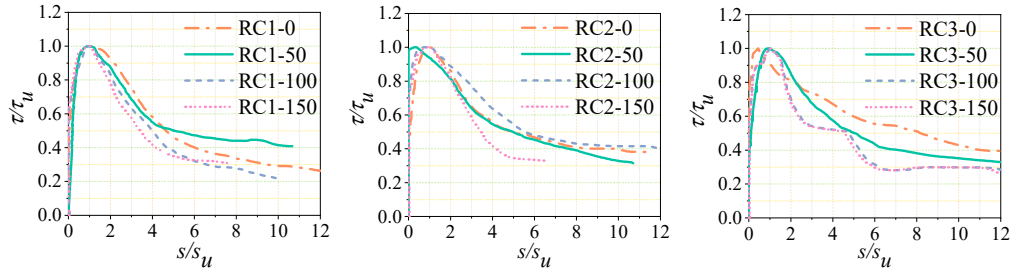


Figure 18. Normalized bond–slip curves of corroded steel reinforcement and RAC after freeze–thaw cycles.

Based on the normalized bond–slip curves in Figure 18 and a previous prediction model proposed by Xiao et al. [64], a modified prediction model was proposed to assess the bond performance under the coupled effect of freeze–thaw cycles and steel reinforcement corrosion, which is expressed as Equation (7).

$$\tau/\tau_u = \begin{cases} [s/s_u]^{\alpha} & (0 \le s \le s_u) \\ \dfrac{s/s_u}{\beta(s/s_u-1)^2+s/s_u} & (s \ge s_u) \end{cases} \quad (7)$$

where α and β are parameters obtained in the ascend and descend sections of the normalized bond–slip curve of RAC severally, and the optimum values were estimated by Equation (7) and tabulated in Table 9.

Table 9. Values of the parameters.

Specimen	α	β
RC1-0	0.31	0.35
RC1-50	0.29	0.31
RC1-100	0.34	0.45
RC1-150	0.32	0.59
RC2-0	0.33	0.32
RC2-50	0.30	0.35
RC2-100	0.30	0.43
RC2-150	0.29	0.57
RC3-0	0.32	0.31
RC3-50	0.29	0.33
RC3-100	0.34	0.40
RC3-150	0.32	0.55

Table 9 indicates that the values of α were randomly distributed in the range of 0.29 to 0.34; thus, the average value of 0.32 was selected as the modified value. Furthermore, β increased with increasing freeze–thaw cycles, while that decreased with an increase in the steel reinforcement corrosion rate. The parameter β was fitted with the freeze–thaw cycles, and the steel reinforcement corrosion rates, and the fitting result is expressed by Equation (8).

$$\beta = 0.348 - 1.375\eta + 0.000003N^{2.27} \qquad R^2 = 0.977 \quad (8)$$

Equations (7) and (8) were superimposed, and the expression of the modified bond–slip prediction model under the coupled effect of freeze–thaw cycles and steel reinforcement corrosion can be obtained and expressed as Equation (9).

$$\tau/\tau_u = \begin{cases} \dfrac{[s/s_u]^{0.32}}{(0.348-1.375\eta+0.000003N^{2.27})(s/s_u-1)^2+s/s_u} & (0 \le s \le s_u) \\ \dfrac{s/s_u}{} & (s \ge s_u) \end{cases} \quad (9)$$

Measured curves and curves fitted by the modified bond–slip prediction model for Equation (9) of 12 specimens were compared in Figure 19, and fitted curves agree well with measured curves.

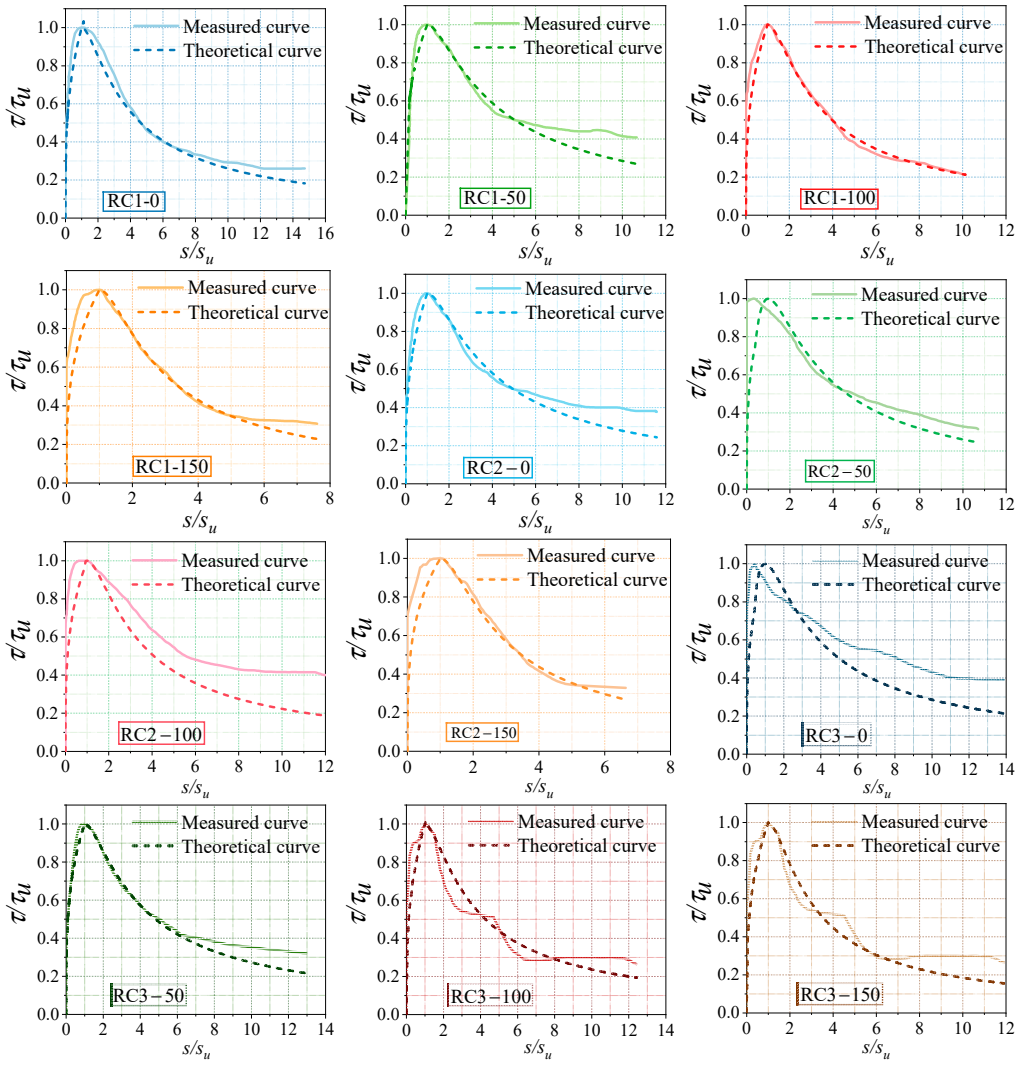


Figure 19. Comparisons of the modified predictions model with the measured bond-slip curves by this study.

The test data of other researchers were collected and aimed to verify the correctness of the modified bond–slip prediction model, which was presented in this paper. Table 10 tabulates details of collected pull-out test results. Measured curves of other researchers and curves fitted by the modified bond–slip prediction model for Equation (9) were compared in Figure 20, and fitted curves agree well with measured curves.

Table 10. Details of the collected pull-out tests results.

References	Freeze–Thaw Cycles	Steel Reinforcement Rate (%)	*d* (mm)	*l* (mm)	Stirrup Involved
Cao et al. [38]	75, 100	0	16	80	No
Alhawat et al. [46]	0	1.61, 4.88	12	60	No
Yang et al. [48]	0	0, 2.1, 2.5	100	20	No
Cao [54]	50, 100	0	80	16	Yes

All pull-out specimens with a 100% replacement ratio of RCA.

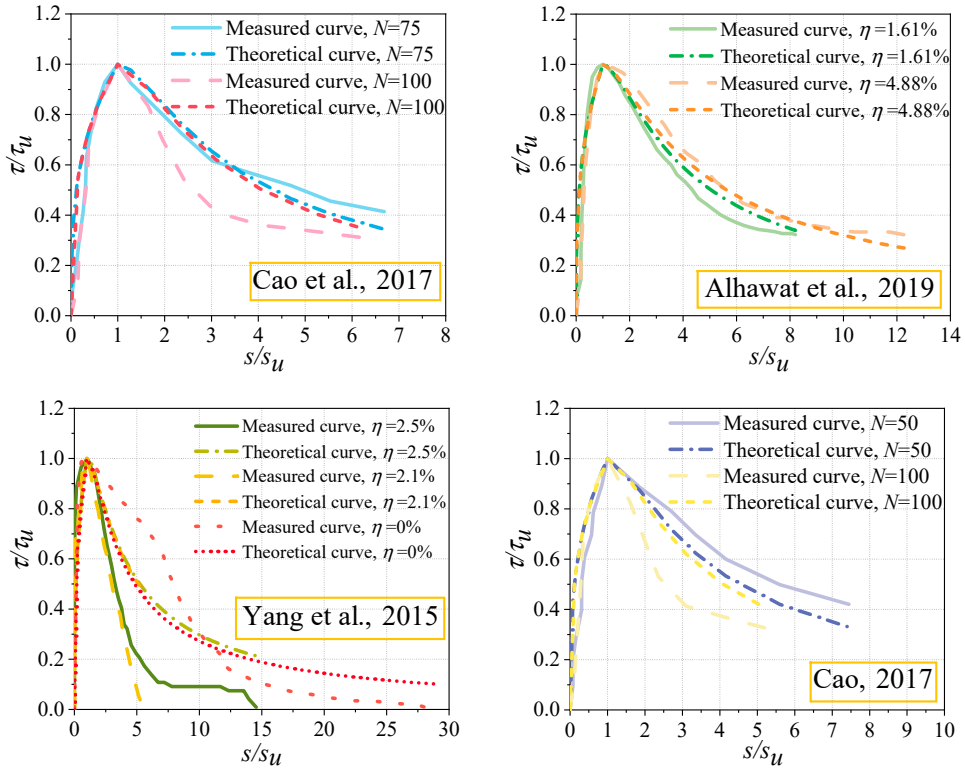


Figure 20. Comparisons of the modified predictions model with the measured bond-slip curves by other researchers (e.g., Cao et al. [38], Alhawat et al. [46], Yang et al. [48], and Cao [54]).

4. Conclusions

In this experiment, experimental and analytical research on the freeze–thaw resistance of RAC (NAC) and the bond performance of corroded steel reinforcement and RAC after freeze–thaw cycles were conducted. The ultimate bond strength and pull-out energy of RAC specimens under the coupled effect of steel reinforcement and freeze–thaw cycles were compared with that under the separate effects of the two factors, respectively. Additionally, the relationships between the ultimate bond strength and different freeze–thaw cycles and steel reinforcement corrosion rates were assessed using the relativity analysis. Finally, a modified bond–slip prediction model of corroded steel reinforcement and RAC after freeze–thaw cycles was established and fitted with the test results of other research to verify its correctness. The principal conclusions are the following:

(1) The freeze–thaw resistance of RAC (NAC) decreased with increasing freeze–thaw cycles, and the freeze–thaw resistance of RAC was inferior to that of NAC.
(2) The failure patterns of RAC and NAC specimens with stirrups were pull-out failures and exhibited no pronounced difference. The coupled effect of freeze–thaw cycles and steel reinforcement corrosion did not alter the failure pattern.
(3) The ultimate bond strength and the pull-out energy decreased with increasing freeze–thaw cycles and steel reinforcement corrosion rates, and that decreased more rapidly under the coupled effect of freeze–thaw cycles and steel reinforcement corrosion.

(4) Based on the results of the relativity analysis, a more pronounced effect of freeze–thaw cycles on the ultimate bond strength compared to that of the steel reinforcement corrosion rates was demonstrated.
(5) A modified bond–slip prediction model of corroded steel reinforcement and RAC after freeze–thaw cycles was presented, which agreed well with the test data of this and other studies.
(6) The freeze–thaw resistance of RAC and the bond performance of corroded steel reinforcement and RAC after freeze–thaw cycles are poorer; thus, the freeze–thaw-resistant design and bond–slip prediction should be of concern to engineers designing RAC structures in a frigid marine environment. Additionally, the enhancement in RAC quality would help alleviate the freeze–thaw damage and bond performance deterioration in RAC structures.
(7) Experimental and analytical research on the freeze–thaw resistance of RAC and the bond performance of corroded steel reinforcement and RAC after freeze–thaw cycles was reported, and the test results contributed to the assessment of RAC structures in a frigid marine environment. The conclusions proposed in this research need to be verified by more test results in the future. Additionally, the effects of the chemical composition of RCA on the freeze–thaw resistance of RAC structures and the effects of other factors (e.g., higher steel reinforcement corrosion rates and different anchoring parameters) on the bond performance of RAC structures need to be considered in future research.

Author Contributions: X.H.: investigation, methodology, writing—original draft preparation; T.S.: writing—review and editing; J.W.: check original draft; F.C.: investigation, methodology, writing—original draft preparation; C.W.: visualization, methodology, formal analysis. All authors have read and agreed to the published version of the manuscript.

Funding: This research was funded by the National Natural Science Foundation of China (No. 51868061), Program of Inner Mongolia Natural Science Foundation (No. 2020MS05071), Foundation of China Postdoctoral Science Foundation (2022M723687).

Institutional Review Board Statement: Not applicable.

Informed Consent Statement: Not applicable.

Data Availability Statement: The data used to support the findings of this study are available from the corresponding author upon request.

Conflicts of Interest: The authors declare that they have no known competing financial interests or personal relationships that could have appeared to influence the work reported in this paper.

References

1. Yildirim, S.T.; Meyer, C.; Herfellner, S. Effects of internal curing on the strength, drying shrinkage and freeze–thaw resistance of concrete containing recycled concrete aggregates. *Constr. Build. Mater.* **2015**, *91*, 288–296. [CrossRef]
2. Qi, B.; Xu, P.; Wu, C. Analysis of the Infiltration and Water Storage Performance of Recycled Brick Mix Aggregates in Sponge City Construction. *Water* **2023**, *15*, 363. [CrossRef]
3. Çelik, A.I.; Özkılıç, Y.O.; Zeybek, Ö.; Karalar, M.; Qaidi, S.; Ahmad, J.; Burduhos-Nergis, D.D.; Bejinariu, C. Mechanical behavior of crushed waste glass as replacement of aggregates. *Materials* **2022**, *15*, 8093. [CrossRef] [PubMed]
4. Qaidi, S.; Najm, H.M.; Abed, S.M.; Özkılıç, Y.O.; Al Dughaishi, H.; Alosta, M.; Sabri, M.M.S.; Alkhatib, F.; Milad, A. Concrete containing waste glass as an environmentally friendly aggregate: A review on fresh and mechanical characteristics. *Materials* **2022**, *15*, 6222. [CrossRef] [PubMed]
5. Basaran, B.; Kalkan, I.; Aksoylu, C.; Özkılıç, Y.O.; Sabri, M.M.S. Effects of waste powder, fine and coarse marble aggregates on concrete compressive strength. *Sustainability* **2022**, *14*, 14388. [CrossRef]
6. Karalar, M.; Özkılıç, Y.O.; Aksoylu, C.; Sabri, M.M.S.; Beskopylny, A.N.; Stel'Makh, S.A.; Shcherban', E.M. Flexural behavior of reinforced concrete beams using waste marble powder towards application of sustainable concrete. *Front. Mater.* **2022**, *9*, 1068791. [CrossRef]
7. Qaidi, S.; Al-Kamaki, Y.; Hakeem, I.; Dulaimi, A.F.; Özkılıç, Y.; Sabri, M.; Sergeev, V. Investigation of the physical-mechanical properties and durability of high-strength concrete with recycled PET as a partial replacement for fine aggregates. *Front. Mater.* **2023**, *10*, 1101146. [CrossRef]

8. Karalar, M.; Bilir, T.; Çavuşlu, M.; Özkiliç, Y.O.; Sabri, M.M.S. Use of recycled coal bottom ash in reinforced concrete beams as replacement for aggregate. *Front. Mater.* **2022**, *9*, 1064604. [CrossRef]
9. Qi, B.; Gao, S.; Xu, P. The application of rubber aggregate-combined permeable concrete mixture in sponge city construction. *Coatings* **2023**, *13*, 87. [CrossRef]
10. Qi, B.; Gao, S.; Xu, P. The application of recycled epoxy plastic sheets waste to replace concrete in urban construction and building. *Processes* **2023**, *11*, 201. [CrossRef]
11. Zhang, Z.; Liang, G.; Niu, Q.; Wang, F.; Chen, J.; Zhao, B.; Ke, L. A Wiener degradation process with drift-based approach of determining target reliability index of concrete structures. *Qual. Reliab. Eng. Int.* **2022**, *38*, 3710–3725. [CrossRef]
12. Li, Z.; Deng, Z.; Yang, H.; Wang, H. Bond behavior between recycled aggregate concrete and deformed rebar after freeze–thaw damage. *Constr. Build. Mater.* **2020**, *250*, 118805. [CrossRef]
13. Zhao, Y.; Lin, H.; Wu, K.; Jin, W. Bond behaviour of normal/recycled concrete and corroded steel bars. *Constr. Build. Mater.* **2013**, *48*, 348–359. [CrossRef]
14. Seara-Paz, S.; González-Fonteboa, B.; Eiras-López, J.; Herrador, M.F. Bond behavior between steel reinforcement and recycled concrete. *Mater. Struct.* **2013**, *47*, 323–334. [CrossRef]
15. Pandurangan, K.; Dayanithy, A.; Prakash, S.O. Influence of treatment methods on the bond strength of recycled aggregate concrete. *Constr. Build. Mater.* **2016**, *120*, 212–221. [CrossRef]
16. Pour, S.M.; Alam, M.S. Investigation of compressive bond behavior of steel rebar embedded in concrete with partial recycled aggregate replacement. *Structures* **2016**, *7*, 153–164. [CrossRef]
17. Wardeh, G.; Ghorbel, E.; Gomart, H.; Fiorio, B. Experimental and analytical study of bond behavior between recycled aggregate concrete and steel bars using a pullout test. *Struct. Concr.* **2017**, *18*, 811–825. [CrossRef]
18. Prince, M.J.R.; Singh, B. Bond behaviour of deformed steel bars embedded in recycled aggregate concrete. *Constr. Build. Mater.* **2013**, *49*, 852–862. [CrossRef]
19. Prince, M.J.R.; Singh, B. Bond strength of deformed steel bars in high-strength recycled aggregate concrete. *Mater. Struct.* **2014**, *48*, 3913–3928. [CrossRef]
20. Dong, H.; Song, Y.; Cao, W.; Sun, W.; Zhang, J. Flexural bond behavior of reinforced recycled aggregate concrete. *Constr. Build. Mater.* **2019**, *213*, 514–527. [CrossRef]
21. Sun, L.; Wang, C.; Zhang, C.; Yang, Z.; Li, C.; Qiao, P. Experimental investigation on the bond performance of sea sand coral concrete with FRP bar reinforcement for marine environments. *Adv. Struct. Eng.* **2022**, *26*, 533–546. [CrossRef]
22. Huang, Y.; Huang, J.; Zhang, W.; Liu, X. Experimental and numerical study of hooked-end steel fiber-reinforced concrete based on the meso- and macro-models. *Compos. Struct.* **2023**, *309*, 116750. [CrossRef]
23. Zhang, W.; Kang, S.; Huang, Y.; Liu, X. Behavior of reinforced concrete beams without stirrups and strengthened with basalt fiber–reinforced polymer sheets. *J. Compos. Constr.* **2023**, *27*, 04023007. [CrossRef]
24. Dong, Z.; Quan, W.; Ma, X.; Li, X.; Zhou, J. Asymptotic homogenization of effective thermal-elastic properties of concrete considering its three-dimensional mesostructured. *Comput. Struct.* **2023**, *279*, 106970. [CrossRef]
25. Rangel, C.S.; Amario, M.; Pepe, M.; Martinelli, E.; Filho, R.D.T. Durability of structural recycled aggregate concrete subjected to freeze–thaw cycles. *Sustainability* **2020**, *12*, 6475. [CrossRef]
26. Liu, K.; Yan, J.; Hu, Q.; Sun, Y.; Zou, C. Effects of parent concrete and mixing method on the resistance to freezing and thawing of air-entrained recycled aggregate concrete. *Constr. Build. Mater.* **2016**, *106*, 264–273. [CrossRef]
27. Wu, J.; Jing, X.; Wang, Z. Uni-axial compressive stress-strain relation of recycled coarse aggregate concrete after freezing and thawing cycles. *Constr. Build. Mater.* **2017**, *134*, 210–219. [CrossRef]
28. Amorim Júnior, N.A.; Silva, G.A.O.; Ribeiro, D.V. Effects of the incorporation of recycled aggregate in the durability of the concrete submitted to freeze–thaw cycles. *Constr. Build. Mater.* **2018**, *161*, 723–730. [CrossRef]
29. Jiang, J.; Yang, H.; Deng, Z.; Li, Z. Bond performance of deformed rebar embedded in recycled aggregate concrete subjected to repeated loading after freeze–thaw cycles. *Constr. Build. Mater.* **2022**, *318*, 125954. [CrossRef]
30. Liu, K.; Yan, J.; Meng, X.; Zou, C. Bond behavior between deformed steel bars and recycled aggregate concrete after freeze–thaw cycles. *Constr. Build. Mater.* **2020**, *232*, 117236. [CrossRef]
31. Shang, H.-S.; Zhao, T.-J.; Cao, W.-Q. Bond behavior between steel bar and recycled aggregate concrete after freeze–thaw cycles. *Cold Reg. Sci. Technol.* **2015**, *118*, 38–44. [CrossRef]
32. Ren, G.; Shang, H.; Zhang, P.; Zhao, T. Bond behaviour of reinforced recycled concrete after rapid freezing-thawing cycles. *Cold Reg. Sci. Technol.* **2019**, *157*, 133–138. [CrossRef]
33. Su, T.; Wu, J.; Yang, G.; Zou, Z. Bond behavior between recycled coarse aggregate concrete and steel bar after salt-frost cycles. *Constr. Build. Mater.* **2019**, *226*, 673–685. [CrossRef]
34. Su, T.; Wang, T.; Wang, C.; Yi, H. The influence of salt-frost cycles on the bond behavior distribution between rebar and recycled coarse aggregate concrete. *J. Build. Eng.* **2022**, *45*, 103568. [CrossRef]
35. Su, T.; Huang, Z.; Yuan, J.; Zou, Z.; Wang, C.; Yi, H. Bond properties of deformed rebar in frost-damaged recycled coarse aggregate concrete under repeated loadings. *J. Mater. Civ. Eng.* **2022**, *34*, 04022257. [CrossRef]
36. Shang, H.; Wang, Z.; Zhang, P.; Zhao, T.; Fan, G.; Ren, G. Bond behavior of steel bar in air-entrained RCAC in fresh water and sea water after fast freeze–thaw cycles. *Cold Reg. Sci. Technol.* **2017**, *135*, 90–96. [CrossRef]

37. Cao, F.; Yin, R.; Wang, C. Beam-type experimental study on bond-slip behavior between recycled concrete and steel bar after freeze-thaw damage. *J. Build. Struct.* **2017**, *38*, 141–148. (In Chinese)
38. Cao, F.; Tang, L.; Ding, B.; Wang, C. Study on bond-slip properties between steel bars and recycled concrete after freeze–thaw cycles. *Eng. Mech.* **2017**, *34*, 244–251. (In Chinese)
39. Wang, C.; Luo, F.; Cao, F.; Lu, L. Bond-slip behavior and constitutive relation of reinforced and recycled concrete after freezing and thawing. *J. Build. Struct.* **2021**, *42*, 214–222. (In Chinese)
40. Tondolo, F. Bond behaviour with reinforcement corrosion. *Constr. Build. Mater.* **2015**, *93*, 926–932. [CrossRef]
41. Lu, Z.-H.; Ou, Y.-B.; Zhao, Y.-G.; Li, C.-Q. Investigation of corrosion of steel stirrups in reinforced concrete structures. *Constr. Build. Mater.* **2016**, *127*, 293–305. [CrossRef]
42. Hou, L.; Liu, H.; Xu, S.; Zhuang, N.; Chen, D. Effect of corrosion on bond behaviors of rebar embedded in ultra-high toughness cementitious composite. *Constr. Build. Mater.* **2017**, *138*, 141–150. [CrossRef]
43. Sanz, B.; Planas, J.; Sancho, J.M. Study of the loss of bond in reinforced concrete specimens with accelerated corrosion by means of push-out tests. *Constr. Build. Mater.* **2018**, *160*, 598–609. [CrossRef]
44. Tariq, F.; Bhargava, P. Post corrosion bond-slip models for super ductile steel with concrete. *Constr. Build. Mater.* **2021**, *285*, 122836. [CrossRef]
45. Zhou, H.; Liang, X.; Zhang, X.; Lu, J.; Xing, F.; Mei, L. Variation and degradation of steel and concrete bond performance with corroded stirrups. *Constr. Build. Mater.* **2017**, *138*, 56–68. [CrossRef]
46. Alhawat, M.; Ashour, A. Bond strength between corroded steel reinforcement and recycled aggregate concrete. *Structures* **2019**, *19*, 369–385. [CrossRef]
47. Alhawat, M.; Ashour, A. Bond strength between corroded steel and recycled aggregate concrete incorporating nano silica. *Constr. Build. Mater.* **2020**, *237*, 117441. [CrossRef]
48. Yang, H.; Deng, Z.; Qin, Y.; Lv, L. A Study on the Bond Behavior of Corroded Reinforced Concrete Containing Recycled Aggregates. *Adv. Mater. Sci. Eng.* **2015**, *2015*, 249301. [CrossRef]
49. Fernandez, I.; Etxeberria, M.; Marí, A.R. Ultimate bond strength assessment of uncorroded and corroded reinforced recycled aggregate concretes. *Constr. Build. Mater.* **2016**, *111*, 543–555. [CrossRef]
50. Liu, S.; Du, M.; Tian, Y.; Wang, X.; Sun, G. Bond behavior of reinforced concrete considering freeze–thaw cycles and corrosion of stirrups. *Materials* **2021**, *14*, 4732. [CrossRef]
51. Zhang, S.; Tian, B.; Chen, B.; Lu, X.; Xiong, B.; Shuang, N. The influence of freeze–thaw cycles and corrosion on reinforced concrete and the relationship between the evolutions of the microstructure and mechanical properties. *Materials* **2022**, *15*, 6215. [CrossRef] [PubMed]
52. *GB175-2007*; Common Portland Cement. China Standardization Administration: Beijing, China, 2007. (In Chinese)
53. *GB8076-2008*; Concrete Admixtures. China Architecture & Building Press: Beijing, China, 2008. (In Chinese)
54. Cao, F. Experimental Study on Mechanical Properties of Recycled Concrete and Bond-Slip between Steel Rebars and Concrete after Freeze–Thaw Cycles. Ph.D. Thesis, Nanjing University of Aeronautics and Astronautics, Nanjing, China, 2017. (In Chinese).
55. *GB/T 50152-2012*; Standard for Experiment Method of Concrete Structures. China Architecture & Building Press: Beijing, China, 2012. (In Chinese)
56. *GB/T 50081-2019*; Standard for Test Methods of Concrete Physical and Mechanical Properties. China Architecture & Building Press: Beijing, China, 2019. (In Chinese)
57. *GB/T 50082-2009*; Standard for Experiment Method of Long-Term Performance and Durability of Ordinary Concrete. China Architecture & Building Press: Beijing, China, 2009. (In Chinese)
58. Zhang, Q.; Li, Y.; Xu, L.; Lun, P. Bond strength and corrosion behavior of rebar embedded in straw ash concrete. *Constr. Build. Mater.* **2019**, *205*, 21–30. [CrossRef]
59. Wang, C.; Wang, Y.; Li, J.; Song, B.; Cao, F. Experimental analysis on bond behavior between recycle concrete and corroded steel bars. *J. Civ. Environ. Eng.* **2016**, *38*, 46–53. (In Chinese)
60. Zhou, H.; Lu, J.; Xv, X.; Dong, B.; Xing, F. Effects of stirrup corrosion on bond–slip performance of reinforcing steel in concrete: An experimental study. *Constr. Build. Mater.* **2015**, *93*, 257–266. [CrossRef]
61. *JTS/T 236-2019*; Technical Specification for Concrete Testing of Port and Waterway Engineering. People's Communications Press Co., Ltd.: Beijing, China, 2019. (In Chinese)
62. Ma, Z.; Zhu, F.; Ba, G. Effects of freeze-thaw damage on the bond behavior of concrete and enhancing measures. *Constr. Build. Mater.* **2019**, *196*, 375–385. [CrossRef]
63. Sam, J. Use of correlation and regression analyses as statistical tools in green concrete research. *GSJ* **2020**, *8*, 991–1004.
64. Xiao, J.; Lei, B. Experimental study on bond behavior between corroded steel bars and recycled concrete. *J. Build. Struct.* **2011**, *32*, 58–62. (In Chinese)

Disclaimer/Publisher's Note: The statements, opinions and data contained in all publications are solely those of the individual author(s) and contributor(s) and not of MDPI and/or the editor(s). MDPI and/or the editor(s) disclaim responsibility for any injury to people or property resulting from any ideas, methods, instructions or products referred to in the content.